J. Fluid Mech. (2004), *vol.* 514, *pp.* 205–230.
DOI: 10.1017/S0022112004000175 Printed in the United Kingdom

Downstream evolution of the most energetic modes in a turbulent axisymmetric jet at high Reynolds number. Part 2. The far-field region

By STEPHAN GAMARD[1], DAEHAN JUNG[2] AND WILLIAM K. GEORGE[3]

[1]Industrial Applications and Healthcare R & D, Praxair Inc., Tonawanda, NY 14150, USA

[2]Department of Mechanical Engineering, Korean Air Force Academy, Cheongwon, Chungbuk 363-849, Korea

[3]Turbulence Research Laboratory, Department of Thermo and Fluid Dynamics, Chalmers University of Technology, Gothenburg, SE-41296, Sweden

(Received 29 May 2002 and in revised form 26 April 2004)

The evolution of the most energetic features in the far-field region of a turbulent axisymmetric jet are investigated by applying the proper orthogonal decomposition (POD) to the double Fourier transform in time and azimuthal direction of the two-point velocity correlations of the streamwise velocity component. Measurements were obtained from 15 to 69 diameters downstream at jet exit Reynolds numbers ranging from 40 000 to 84 700 using two different experimental techniques, an array of 139 long hot wires and an articulated array of 15 hot wires.

The POD eigenspectra for the far jet were found to follow equilibrium similarity scaling sooner than the single-point statistics. The first POD eigenspectrum accounts for more than 50% of the resolved streamwise energy, and has three major peaks: a dominant one at azimuthal mode-2 for near-zero frequency, another at mode-1 at a constant local Strouhal number, $f\delta_{1/2}/U_c$, and a third smaller one for azimuthal mode-0 at near-zero frequency. The eigenspectra were independent of downstream position, but similar to those obtained as early as $x/D = 6$ in Part 1 of this paper. All the eigenspectra integrated over frequency peaked at azimuthal mode-2.

1. Introduction

Due to its geometrical simplicity and the ease with which it can be generated, the axisymmetric jet has been extensively studied over the years. From the perspective of stability theories, the homogeneous jet is believed to be 'marginally globally stable (in its entire flow field), with local velocity profiles being locally convectively unstable in the entire field, but absolute temporally growing instability is possible at some streamwise position. In those cases, the global modes are often damped in time, but they can be preferentially destabilized by applying an external forcing at the appropriate frequency' (Huerre & Monkewitz 1990). Since Batchelor & Gill (1962), it has been widely believed that azimuthal mode-1 instabilities should dominate the far jet. Although these stability analyses were based on linearization of the governing equations, there has long been the suspicion that the results could be applied to turbulence as well if the mean velocity profile were substituted for the base flow. For the far jet, there has been considerable support for this view, at least until very recently. Appendix A provides a brief historical review.

Using the exhaust plume of a TITAN IV rocket fired in the upward direction, Mungal & Hollingsworth (1989) confirmed the presence in the far region of organized structures at very high Reynolds number, 2×10^8. At low Reynolds number (about 500–600), Dimotakis, Miake-Lye & Papantoniou (1983) investigated the evolution of coherent structures in the far field of an axisymmetric jet up to 160 diameters using laser-induced fluorescence, and concluded that they were dominated by axisymmetric (mode-0) or helical (mode-1) modes. Using planar flow visualizations and concentration field measurements at the relatively low Reynolds numbers of 1000 to 5000, Yoda, Hesselink & Mungal (1992, 1994) observed both axisymmetric and helical modes and concluded that the structures were evolving as a pair of counter-rotating spirals, or ± 1 modes. Finally, Tso & Hussain (1989), using an array of hot wires in the far field of a round jet at high Reynolds number, $Re_D = 69\,000$, also deduced the dominance of helical modes. Their apparatus, however, (a rake of hot-wires at 0° with two extra probes at 90° and 270°) could only account for axisymmetric (mode-0), helical ($m = \pm 1$), and double-helical ($m = \pm 2$) structures, so any higher spatial modes would have been aliased into the lower ones.

In order to reconstruct the streamwise velocity component from the proper orthogonal decomposition (POD) modes in an axisymmetric jet mixing layer, Citriniti & George (2000) designed an array of 138 hot wires to measure a cross-section of the flow field simultaneously. The instantaneous flow field was projected back onto the POD eigenfunctions to determine the coefficients, so that the flow could be reconstructed, as a whole or in part. These velocity reconstructions at three diameters downstream of the jet exit provided evidence for both azimuthally coherent 'volcano-like' events that contained most of the energy, and counter-rotating, streamwise vortex pairs (or ribs) in the region between successive azimuthally coherent structures. Using the same apparatus, Jung, Gamard & George (2004) in Part 1 of this work extended the application to the full near-field region of the axisymmetric jet from two to six diameters downstream at high Reynolds numbers. They showed that the energy distribution changed with downstream distance. Azimuthal mode-0, which dominated the flow field near the jet exit, was overwhelmed by the end of the potential core by higher azimuthal modes with very low frequency content. By six diameters, azimuthal mode-2 was the dominant mode. The velocity reconstructions showed that, concurrent with the diminution of the axisymmetric mode, the most energetic feature of the flow changed from a 'volcano-type' event to a 'propeller-type' event where most of the energy was in a mode-2 pattern for the entire extent of the shear layer. In fact, as first reported by Gamard *et al.* (2002) (and in substantially more detail herein), there appears to be no further evolution of the POD azimuthal distribution farther downstream. This dominance of mode-2 in the far jet has recently been confirmed by the POD applied to DNS by Freund & Colonius (2002) and in noise measurements by Kopiev *et al.* (1999) and Kopiev (2001, personal communication).

This paper reports on a detailed application of the POD to the far jet. The preliminary findings of mode-2 dominance by Gamard *et al.* (2002) are confirmed. Also, the results are shown to be independent of Reynolds number and methodology, and consistent with multi-point equilibrium similarity of the far jet.

2. Experimental apparatus

2.1. *The turbulent jet*

The probe arrays used in this experiment were of fixed size and could not be adjusted easily to accommodate different shear layer widths. Therefore in order to measure at

a large range of downstream positions and still have adequate lateral coverage, jets of different diameters were used to cover the same relative portion of the flow field at different downstream positions (as measured by x/D).

2.2. *The large jet*

The large turbulent jet has been extensively used in the past by the Turbulence Research Laboratory in Buffalo, and is therefore thoroughly described in previous dissertations (Glauser 1987; Jung 2001), and in Part 1 of this paper. A second contraction was fitted at the end of the nozzle to create an exit diameter of 2.54 cm. The new contraction, 10 cm in length, was machined to fit very tightly to the contraction nozzle, and also designed to a fifth-order polynomial curve to match the curvature at the point of attachment without any discontinuity. At a downstream distance of 1 cm ($x/D = 0.4$) the mean velocity profile is flat with no discernible overshoot, and has a 1.2 mm thick boundary layer with less than 1% turbulence intensity.

2.3. *The 1 cm jet*

Even by reducing the contraction to 2.54 cm diameter, the probe array did not provide enough coverage of the flow field to apply the POD over a distance of more than 35 diameters downstream. A second jet facility was therefore used in this experiment with a 1 cm exit diameter and exit velocities up to 70 m s^{-1}. It allowed measurements with the fixed array up to 69 diameters downstream. The jet facility consisted of a cubic box of dimensions $58.5 \times 58.5 \times 59$ cm^3, with an entrance for the pressurized air on one side, and a 1 cm exit diameter nozzle following a fifth-order polynomial curve on the other. Air was supplied from a high-pressure tank located outside the premises, and injected directly into the box via a high-pressure valve. The jet was allowed to run for several hours before taking any measurements to allow the long starting transient of the piping and compressor system to die out.

2.4. *The measuring devices*

In direct continuation of the previous near-field measurements described in Part 1, an array of 139 long hot wires was used. A second set of experiments utilized a simplified (but adjustable) array of 15 hot wires, both to be sure that the large array was not adversely affecting the measurements, and to investigate the sensitivities of the POD to the exact region covered by the array.

2.4.1. *The 139-hot-wire array*

The first set of data, hereafter referred to as the UB data† used an 139-hot-wire array, shown in figure 1. The array is the same as in Part 1 (see also Citriniti & George 1997, 2000) except that a centre wire was added to obtain the centreline velocity directly. The centre wire was 5 mm long with the same diameter as the other ones, 12.7 μm, and was connected to a standard Dantec 55M10 constant-temperature anemometer. During the last sets of data with the 1 cm jet, this wire broke. Unfortunately, this was not noticed until the last set of data was processed, so for this data set the centreline velocity was inferred by curve-fitting the entire profile as described later.

2.4.2. *The 15-hot-wire array*

Because of the surprising nature of the earlier results (the dominance of azimuthal mode-2, see Gamard *et al.* 2002), it was decided to re-measure the same jet using a

† These measurements were made at SUNY/Buffalo prior to moving the facility to Chalmers.

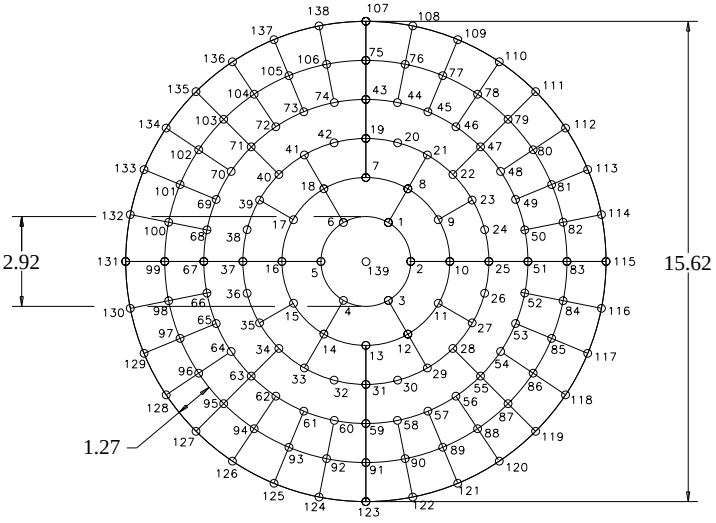

FIGURE 1. The 139-hot-wire probe array. Each dot represents a single hot-wire. Dimensions are in cm.

simpler array of probes to ensure that our results were not an artifact of the 139-probe array. Therefore a second experiment was conducted using the same large jet described in § 2.1 equipped with the 2.54 cm nozzle. The data are collectively referred to as CTH data.† The downstream measurement span was from 15 to 35 diameters at an exit velocity of 50 m s^{-1}. Measurements of the streamwise component of the velocity were obtained using a rake of 15 single hot wires mounted on two wings, one moveable azimuthally around the other in 15° increments. The wires were aligned along concentric circles to minimize the cross-flow errors, see figure 2. The 3 mm long hot wires were made of 5 μm unplated tungsten and connected to DANTEC miniature-CTA 54T30 anemometers. The signal was low-passed at 1 kHz (in the inertial subrange) with the filter inherent to the anemometers, since only the large scales were of interest in this study. The signal was then sent to an IO Tech Wavebook 516 16 bit 1 MHz data acquisition board and processed via an IO Tech acquisition card controlled by National Instrument Labview routines. Each signal was sampled simultaneously at a 4 kHz frequency rate with 4096 scans per block. Table 1 presents a summary of all the experimental conditions.

3. The 'slice' POD decomposition

The mathematics and physics underlying the application of the proper orthogonal decomposition (or POD) have been described in numerous places, e.g. Part 1 or Holmes, Lumley & Berkooz (1996) and George (1988, 1999). The highlights will be briefly reviewed, since the symbols and terminology are essential to understanding the data presented later.

As in Part 1, the slice-POD is applied to the doubly transformed (in the azimuthal direction and time) velocity at a cross-section of the flow at a given downstream position, x (which remains a parameter in the decomposition). For the single velocity

† The facility had been moved to Chalmers.

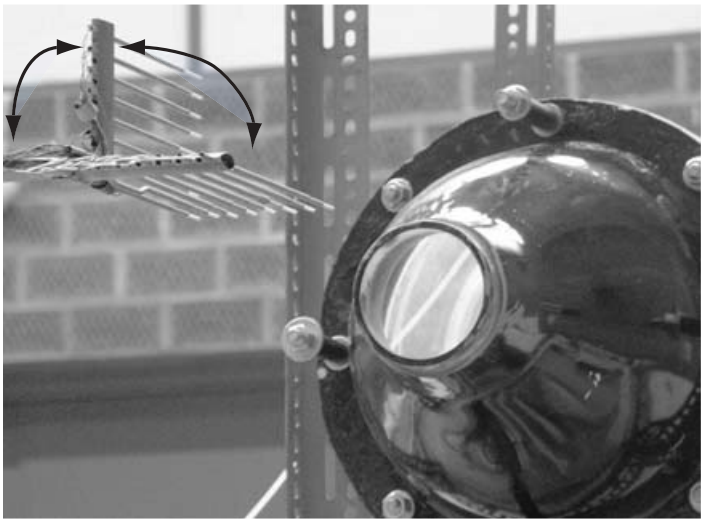

FIGURE 2. The 15-hot-wire array in front of the 9.8 cm jet exit. Moveable wing at 90°.

	139-hot-wire array (UB data) 2.54 cm diameter						1 cm diameter					
x/D	20		21		22		46		54		69	
U_0 (m s^{-1})	40	50	40	50	40	50	60	70	60	70	60	70
$Re_D(\times 10^{-3})$	67.7	84.7	67.7	84.7	67.7	84.7	40.0	46.7	40.0	46.7	40.0	46.7
	15-hot-wire array (CTH data) 2.54 cm diameter											
x/D	15	20	25	30	35							
U_0 (m s^{-1})			50									
$Re_D(\times 10^{-3})$			84.7									

TABLE 1. Summary of experimental conditions.

component considered here, the POD integral equation becomes

$$\int R_{x,x}(x;r,r',m,f)\phi_x^{(n)}(x,r',m,f)r'\mathrm{d}r' = \lambda^{(n)}(m,f;x)\phi_x^{(n)}(x,r,m,f), \qquad (3.1)$$

where $R_{x,x}(x;r,r',m,f)$ is the two-point cross-spectral tensor of the streamwise velocity component, the $\lambda^{(n)}(m,f;x)$ are eigenvalues (or more properly eigenspectra), and the $\phi_x^{(n)}(x,r,m,f)$ are eigenfunctions, for each POD mode, n, which are functions of azimuthal mode number, m, frequency, f, with the latter also a function of radial direction, r.† In practice n and m are limited by the number of radial and azimuthal grid points, respectively.

The eigenspectra are ordered, i.e. $\lambda^{(1)} > \lambda^{(2)} > \lambda^{(3)} \ldots > 0$. Also, if the POD eigenspectra are summed, integrated over all frequencies, and summed over all

† Actual implementation of the decomposition is slightly altered by the presence of the Jacobian, r. See Part 1 or Citriniti & George (2000) for details.

azimuthal modes, the result is equal to the streamwise component of the turbulence kinetic energy integrated over the cross-section, i.e.

$$E \equiv \sum_n \sum_m \int_f \lambda^{(n)}(m, f; x)\, \mathrm{d}f. \tag{3.2}$$

In the following sections a number of partial sums and integrals of equation (3.2) will be considered.

The symmetry properties of the kernel $R_{x,x}$ for the axisymmetric jet considered here were discussed in detail in Appendices A and B of Part 1. The results can be briefly summarized as follows: the eigenspectra, $\lambda^{(n)}(m, f; x)$, are the same in all four quadrants, i.e. quadrant II ($m > 0,\ f < 0$), quadrant III ($m < 0,\ f < 0$), and quadrant IV ($m < 0,\ f > 0$) are the same as for quadrant I ($m > 0,\ f > 0$). The eigenfunctions differ slightly in that in quadrants I and II they are the same, while in I and III they are complex conjugates, as they are in quadrants II and IV. Because of this, only data for $m > 0,\ f > 0$ will be presented below.

The two different numerical implementations

The handling of the azimuthal decomposition varied slightly for the two different arrays used. For all setups, the velocity signal from each hot wire was first sampled, then Fourier transformed in time using an FFT. For the 139-hot-wire array where the data at all positions were acquired simultaneously, the velocity Fourier coefficients were computed from the incoming data using an FFT. These were then Fourier transformed azimuthally for each radius and the cross-spectra computed directly. For the 15-hot-wire array, on the other hand, the temporal cross-spectra were acquired in twelve steps, with the moveable wing azimuthally separated sequentially from the fixed one by increments of 15° from 15° to 180°. The azimuthal and temporal cross-spectra were then computed at each radius by combining the different angular positions and by using symmetry around the axis to account for the other half of the cross-section. The symmetry was verified by the earlier results obtained from the 139-hot-wire array, as presented in Gamard *et al.* (2002).

Aside from the operations performed, the major difference between the two setups is that the number of azimuthal modes resolved is 12 for all radial positions with the 15-hot-wire array, while for the 139-hot-wire array it is different for every radius (3 for the first one, 6 for the second, 12 for the third, and 16 for the last three). The second experiment therefore allowed a confirmation that the azimuthal decomposition using the 139-hot-wire setup was adequate, and vice versa.

4. Single-point results

The equations of the far-field region of the momentum-conserving jet (with no co-flowing stream) are known to admit equilibrium similarity solutions (George 1989, and Appendix C of Hussein, Capp & George 1994). In particular, for the mean velocity and turbulence intensity:

$$U(x, r) = U_c(x)\ f(\eta), \tag{4.1a}$$

$$\overline{u^2}(x, r, \theta, t) = (U_c(x))^2\ g(\eta, \theta, t), \tag{4.1b}$$

where $\eta = r/\delta_{1/2}(x)$, $\delta_{1/2} \propto (x - x_0)$ is the shear layer width at which the velocity is half its centreline value, and x_0 is the virtual origin. The centreline velocity U_c is inversely proportional to the jet shear layer width, $\delta_{1/2}$, since the jet is a

constant-Reynolds-number evolving flow. The results have been shown by many to describe real jets if they are not affected by confinement (Hussein *et al.* 1994; Panchapakesan & Lumley 1993). Consistent with the theory, the recent studies of Mi, Nobes & Nathan (2001) confirm a weak dependence on upstream conditions, as do the relatively low DNS results of Boersma, Brethouwer & Nieuwstadt (1998). Ewing & George (1995) extended the single-point analysis by applying equilibrium similarity considerations to the two-point equations for the jet (see also Ewing 1995), but the theory has never been subjected to experimental tests due to the lack of measurements of the two-point quantities. This latter analysis is of interest in § 6 below.

The measurements reported here (especially those with the long wires) were not aimed at producing model-verification-quality single-point statistics, but were instead optimized for the resolution of the large scales and to avoid aliasing in the spatial transforms. Nonetheless, the single-time single-point statistics can be compared with the data of Hussein *et al.* (1994), who present curve fits for stationary hot wires (HW), for LDA, and one for their flying hot wire (FHW) measurements. The fit for the LDA/FHW is the closest to the real velocity field in the jet; however, we used the HW curve fits, because they are the closest ones to our technique (the difference being mainly in the cutoff induced by the wire size and the low-pass filtering).

For the data with the missing centreline probe, the centreline velocity (along with the virtual origin) was obtained by best-fitting the velocity profile data with the recommended analytical curves. The data sets for the different jets were analysed separately since the constants are directly related to the initial conditions. These estimations were in excellent agreement with the actual measured value at the centreline when it was available. The mean velocity profiles in figure 3 show excellent collapse inside $r/\delta_{1/2} < 1.2$, and are close to the profiles of Hussein *et al.* (1994). Outside this the UB data from the most upstream positions are slightly higher. The reason for this is not understood, but perhaps is traceable to the calibration at low velocities.

The turbulence intensities measurements from the UB data, figure 4(*a*), show clearly the reduced energy due to the cutoff from the length of the wires, exactly as expected (Citriniti & George 1997). The CTH data also are lower than those of Hussein *et al.* (1994), especially near the centreline where the convection velocity is the highest, consistent with the fact that the data were low-pass filtered at 1 kHz.

As mentioned in Part 1, application of the POD to the jet requires the two-point cross-spectra to be weighted by the Jacobian of the cylindrical coordinate system. Thus one measure of the array coverage is how well $r\overline{u_x^2}$ is resolved, since it can be integrated with respect to r to obtain the total turbulence kinetic energy in the flow (to within a factor of 2π). This integrand is plotted in similarity variables in figure 4(*b*), and compared with the estimate obtained from Hussein *et al.* (1994). Table 2 summarizes the differing coverages and resolutions of the flow field by tabulating the integrals of the curves in figure 4(*b*) normalized by the integrals computed using the HW curve-fit of Hussein *et al.* (1994). There are two reasons for values below 100%: spatial filtering by the wires and inadequate radial array coverage. The smaller values obtained by the 139-wire array, as noted above, are due to the filtering of the small scales by the spatial filtering of the long wires, so are not of concern. Inadequate radial coverage would be a major concern, however, since it could skew the results from one mode to another, depending on what information is missing. From the figure it is clear that all but one of the array configurations resolve the flow to at least $r/\delta_{1/2} \approx 1.5$. The effect of reduced area coverage on the POD will be considered below and in Appendix B.

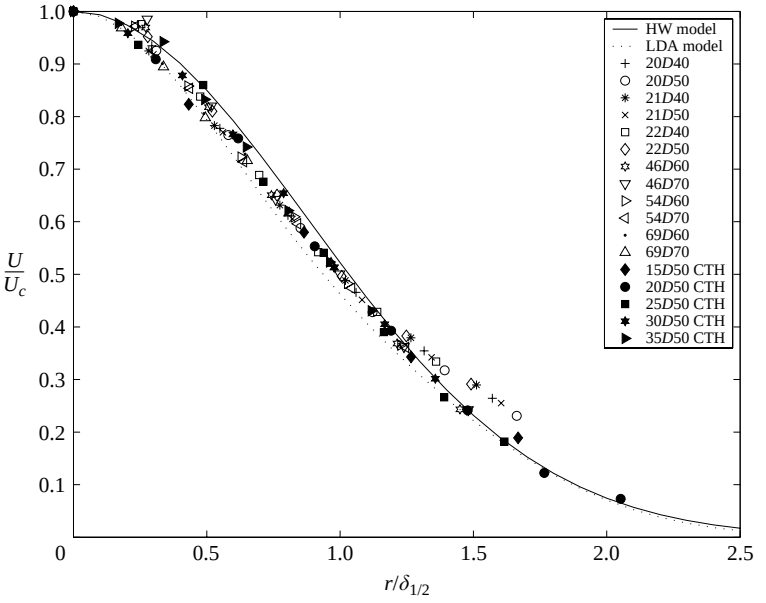

FIGURE 3. Mean velocity profiles in similarity variables. The experimental conditions for each symbol are given in table 1. The two curve-fits, LDA and single hot-wire (HW), are taken from Hussein *et al.* (1994).

139-hot-wire probe array (UB data)	20D 40 m s^{-1}	55.3%
	20D 50 m s^{-1}	61.1%
	21D 40 m s^{-1}	52.6%
	21D 50 m s^{-1}	59.6%
	22D 40 m s^{-1}	49.5%
	22D 50 m s^{-1}	58.3%
	46D 60 m s^{-1}	46.4%
	46D 70 m s^{-1}	49.7%
	54D 60 m s^{-1}	34.1%
	54D 70 m s^{-1}	37.0%
	69D 60 m s^{-1}	21.1%
	69D 70 m s^{-1}	22.6%
15-hot-wire probe array (CTH data)	15D 50 m s^{-1}	83.5%
	20D 50 m s^{-1}	102.3%
	25D 50 m s^{-1}	96.5%
	30D 50 m s^{-1}	85.2%
	35D 50 m s^{-1}	67.4%

TABLE 2. Percentage of coverage of the POD integral kernel when compared to Hussein *et al.*'s (1994) model for hot-wire measurements.

5. The eigenspectra

5.1. *General features*

Using the two-point cross-spectra as kernel, the integral equation (3.1) was solved at a fixed cross-section as described in § 3. The resulting eigenspectra, $\lambda^{(n)}(m, f; x)$, show

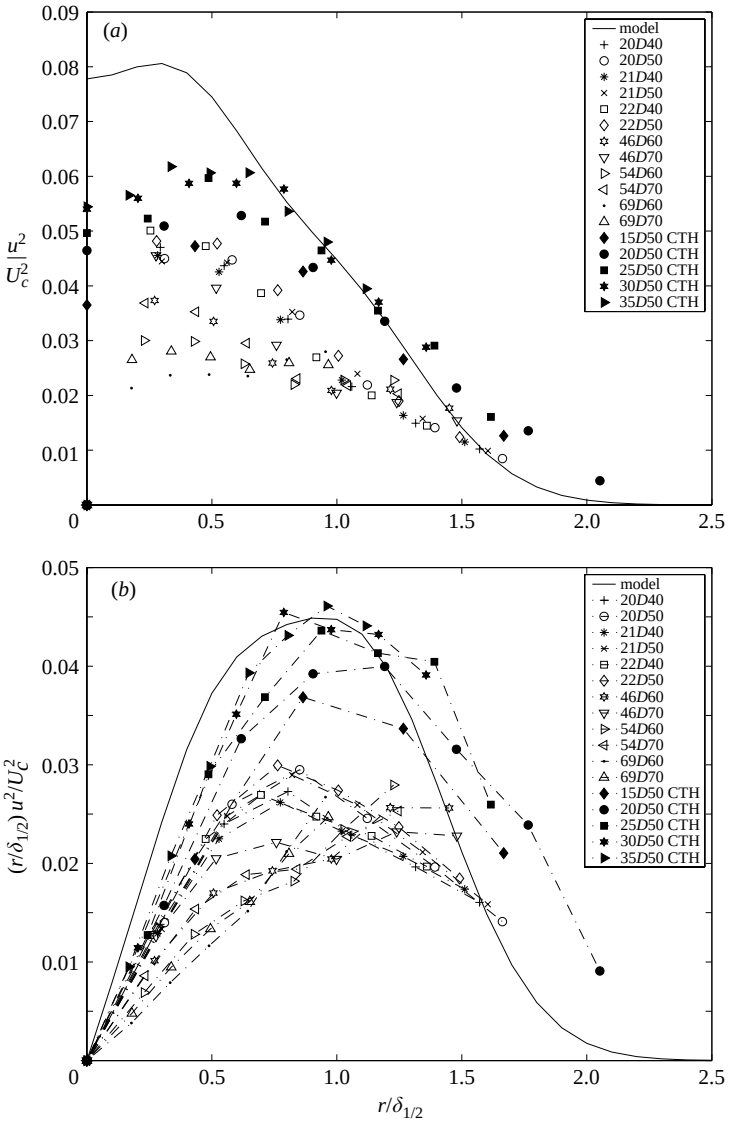

FIGURE 4. (*a*) Turbulence intensity profiles in similarity variables along with empirical curve fits taken from Hussein *et al.* (1994). The 'missing' energy for the UB data is due to the small-scale energy removed by the long wires which varies with Reynolds number and downstream position, or due to low-pass filter in the case of the CTH data. (*b*) Integrands of the flow turbulence kinetic energy in similarity variables. Areas under curves are the total streamwise turbulence kinetic energy in the flow.

how the streamwise component of the turbulence kinetic energy is distributed with azimuthal mode number, m, and frequency, f, at a given downstream position, x. The first eigenspectrum contains more than 60% of the flow energy for the 139-wires data, and more than 50% for the CTH data, consistent with the results of Citriniti & George (2000) and Part 1, and makes clear the ability of the POD to extract the most energetic features of the flow. (Note that the term 'energy' hereafter refers only to the streamwise component of the turbulence kinetic energy, since the apparatus is designed to measure only it.)

	$\lambda^{(n)}$						Energy
n	1	2	3	4	5	6	($m^4 s^{-2}$)
20D 40 m s^{-1}	63.6	19.2	9.4	4.8	2.1	0.8	0.0169
20D 50 m s^{-1}	63.2	19.5	9.5	4.8	2.1	0.8	0.0265
21D 40 m s^{-1}	63.6	19.2	9.4	4.9	2.2	0.8	0.0164
21D 50 m s^{-1}	63.1	19.5	9.5	5.0	2.2	0.8	0.0231
22D 40 m s^{-1}	63.5	19.3	9.4	4.9	2.2	0.8	0.0159
22D 50 m s^{-1}	63.5	19.1	9.5	4.9	2.2	0.8	0.0256
46D 60 m s^{-1}	61.4	19.7	10.0	5.4	2.6	1.0	0.00579
46D 70 m s^{-1}	62.0	19.6	9.8	5.2	2.5	1.0	0.00766
54D 60 m s^{-1}	62.7	19.1	9.6	5.1	2.4	1.0	0.00489
54D 70 m s^{-1}	62.7	19.2	9.6	5.1	2.4	1.0	0.00644
69D 60 m s^{-1}	64.5	18.9	8.9	4.6	2.2	0.9	0.00369
69D 70 m s^{-1}	64.3	19.2	8.9	4.6	2.2	0.9	0.00486

TABLE 3. Relative percentage per POD mode number, and total turbulence kinetic energy per configuration. Data from the 139-hot-wire array.

	$\lambda^{(n)}$							Energy
n	1	2	3	4	5	6	7	($m^4 s^{-2}$)
15D 50 m s^{-1}	53.9	21.2	11.8	7.3	3.4	1.9	0.5	0.0125
20D 50 m s^{-1}	51.5	19.8	11.9	7.8	4.8	2.7	1.4	0.0116
25D 50 m s^{-1}	51.6	18.8	11.4	7.5	5.3	3.5	2.0	0.00974
30D 50 m s^{-1}	53.9	18.3	10.5	6.8	5.0	3.5	2.1	0.00834
35D 50 m s^{-1}	54.5	19.0	10.1	6.5	4.7	3.2	2.0	0.00703

TABLE 4. Relative percentage per POD mode number, and total turbulence kinetic energy per configuration. Data from the 15-hot-wire array.

The energy contribution per POD mode number for each configuration is presented in table 3 for the UB data. As can be seen from the differences in total turbulence kinetic energy picked by the array, the actual percentages are surprisingly consistent for each configuration, especially considering the different Reynolds numbers and varying coverage of the flow field. This lends considerable support to the arguments presented in § 4 that the resolution and spatial coverage of the array are adequate, and that the Reynolds number of the jet is high enough to be nearly irrelevant. The smaller hot wires, table 4, pick up relatively less of the turbulence kinetic energy in the first POD mode, as expected since the denominator is increased by the reduced spatial filtering compared to the 139-hot-wire array.

The eigenspectra, figure 5, show that the energy is concentrated at very low frequencies (less than 100 Hz) and in only a few azimuthal mode numbers. All show a dominant peak in amplitude at very low frequency for azimuthal mode-2, and a secondary peak at a higher frequency for azimuthal mode-1. A third peak at azimuthal mode-0 for near-zero frequency is also present in some cases. The latter is lost when the coverage of the flow field by the array is not adequate (see Appendix B). It also seems that it is not picked up by the long wires of the UB measurements with the 2.54 cm jet exit diameter, but is definitively there when using the smaller wires.

The resemblance of the different eigenspectra to each other can be directly related to the equilibrium similarity theory for this flow. As shown in Gamard *et al.* (2002),

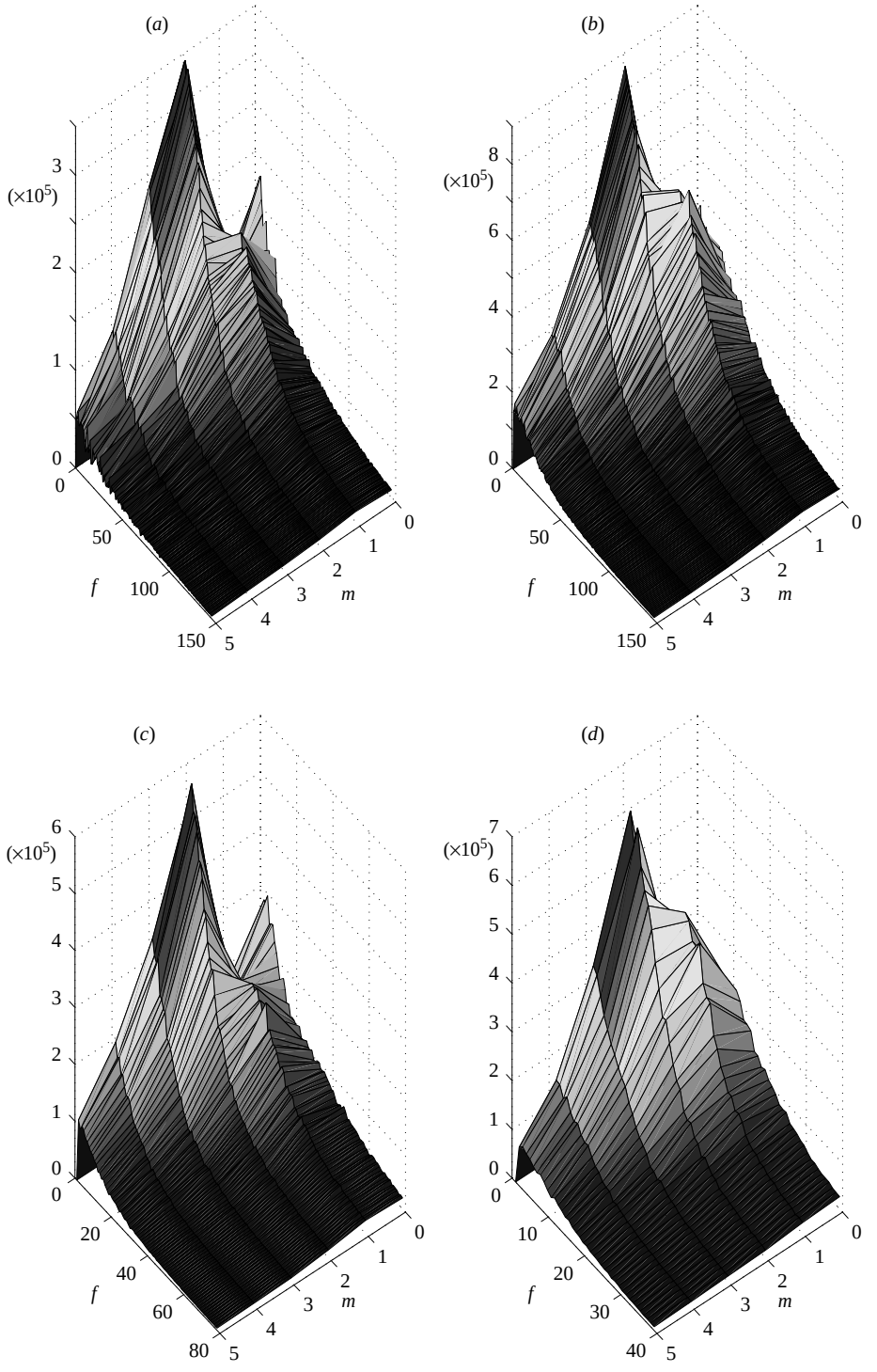

FIGURE 5. First POD mode eigenspectra as function of azimuthal mode number (m) and frequency at different downstream positions. CTH data: (a) $x/D = 20$, $U_0 = 50\ \mathrm{m\,s^{-1}}$. UB data: ($b$) $x/D = 21$ at $U_0 = 50\ \mathrm{m\,s^{-1}}$, ($c$) $x/D = 46$ and (d) 69 at $U_0 = 70\ \mathrm{m\,s^{-1}}$.

when normalizing the frequency using the local Strouhal number, $St = fx/U_c$, where U_c is the centreline velocity, the peak at azimuthal mode-1 in the eigenspectra is at a Strouhal number of approximately 1.

As noted also in Part I, the high turbulence intensity of this flow precludes the simple application of Taylor's frozen field hypothesis to the experimental results. Because of the unsteady convection velocity and the strong mean shear, 'frequency' cannot be simply interpreted as temporal or spatial, but is a combination of both (Lumley 1965). Or, in other words, it is not obvious what the proper convection velocity is without detailed spatial and temporal measurements with streamwise separation (cf. Wills 1964; Zaman & Hussain 1981; George, Hussein & Woodward 1989). Even so it is reasonable to infer that the peak for azimuthal mode-1 is a convected disturbance. The peaks at near-zero frequency, however, are probably not, since otherwise they would correspond to disturbances of a few metres long, which is clearly unphysical.

5.2. *Energy distribution per mode number*

The energy distribution per azimuthal mode number, m, is given by

$$\xi^{(n)}(m;x) = \frac{\displaystyle\int_f \lambda^{(n)}(m,\, f\,;x)\,\mathrm{d}f}{\displaystyle\sum_m \int_f \lambda^{(n)}(m,\, f\,;x)\,\mathrm{d}f} \tag{5.1}$$

where the denominator is actually the total streamwise turbulence kinetic energy for the downstream component of the velocity according to (3.2). The results are shown in figure 6 for the first eigenspectrum ($n = 1$). It was expected that the results would not change far downstream, since they are described by equilibrium similarity. It seems, however, that the eigenspectra exhibit similar characteristics well before equilibrium similarity applies to the single-point statistics (typically $x/D = 20$ to 30). Although the modal evolution (described in detail in Part 1) from a state dominated by axisymmetric mode-0 at $x/D = 2$ is not quite complete by $x/D = 6$, the latter position clearly exhibits a dominance of azimuthal mode-2, with the peak located near zero frequency. The minor differences between the profiles thereafter are due to the experimental conditions, mainly the differences in coverage of the cross-section of the flow by the probe array, and the change in scales experienced by the wires.

Thus these POD eigenspectra (integrated over frequency) peak at azimuthal mode-2, and not at mode-1. Prior to the first presentation of our results (Gamard *et al.* 2002), this had not been reported before, and appears to contradict earlier experiments using flow visualization (Dimotakis *et al.* 1983; Yoda *et al.* 1992, 1994) and conditional sampling (Tso & Hussain 1989). Mode-2 dominance has been confirmed (as noted earlier) in low Reynolds number DNS (Freund & Colonius 2002) and in the radiated noise field beyond $x/D = 5$ (V. F. Kopiev 2001, personal communication). The extensive results reported herein make clear beyond reasonable doubt that the mode-2 phenomenon is real, independent of facility, methodology, and Reynolds number (at least over the range of these experiments).

Concerning the earlier experimental results of others, it is likely that the conditional sampling experiments lacked the resolution to measure more than a few azimuthal modes. Since there was no spatial filtering prior to sampling, the unresolved modes were aliased into the lower ones, thereby distorting the low-mode-number energy distribution. Further complicating this is the fact that azimuthal mode-2 is at near-zero frequency, and could easily have been overlooked or considered unphysical, especially

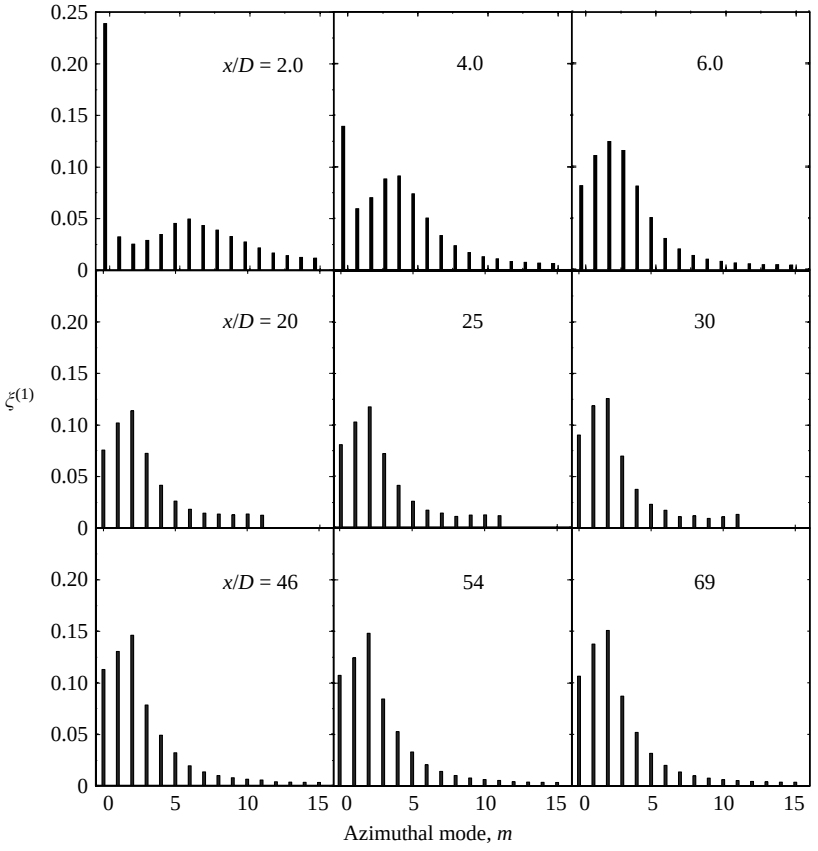

FIGURE 6. Relative fraction of energy contained in the first eigenspectrum as a function of mode number. First row, near-field results (Part 1), second row 2.54 cm jet with 15-hot-wire array, third row 1 cm jet with 139-hot-wire array.

if a convected instability were expected. Also, as seen in § 7, the corresponding eigenfunctions do not peak at the same radial position, therefore using too few probes can definitely alter the results. In fact, as will be shown in § 7, all of the eigenfunctions change sign at different radii; so it would even be possible to completely miss the contribution of one or more modes by measuring at only one radial location (as in most previous hot-wire experiments), in particular near where it is zero.

6. The eigenspectra in two-point similarity variables

The two-point velocity correlation equations for the axisymmetric jet have been shown to admit to equilibrium similarity solutions (Ewing 1995; Ewing & George 1995). Since the POD decomposition is always made at a fixed downstream position, it is the two-time, two-point (but single x location) cross-spectra that are of interest. Normally the two-time (or frequency) variable would be difficult to scale because of the failure of Taylor's hypothesis. In the case of the far jet, this problem is resolved by the fact that both the convection velocity (whatever it is) and the turbulence intensities must scale with the centreline velocity, U_c. The only other local parameter is the half-width, $\delta_{1/2}$. It is easy to show from the definining integral, equation (3.1),

x/D	20		21		22		46		54		69	
U_0 (m s^{-1})	40	50	40	50	40	50	60	70	60	70	60	70
$K \times 10^4$	3.90	4.24	4.03	3.53	3.50	3.98	3.46	3.60	2.74	2.85	1.84	1.93

TABLE 5. Ratio K of total downstream turbulence kinetic energy measured in the corresponding cross-section to $(U_c\delta_{1/2})^2$. 139-hot-wire array data (UB).

x/D	15	20	25	30	35
U_0 (m s^{-1})	50	50	50	50	50
$K \times 10^4$	2.81	2.24	1.79	1.44	1.27

TABLE 6. Ratio K of total downstream turbulence kinetic energy measured in the corresponding cross-section to $(U_c\delta_{1/2})^2$. 15-hot-wire array data (CTH).

that the appropriate similarity scaling for the eigenspectra, $\lambda^n(m, f; x)$, is

$$\Lambda^{(n)}\big(m, \delta_{1/2} f/U_c; x/D\big) = \frac{\lambda^{(n)}(m, f; x)}{U_c \delta_{1/2}^3}. \tag{6.1}$$

It is not useful, however, to apply this scaling directly, because (as noted earlier) the probe arrays do not measure the full streamwise kinetic energy at a cross-section. In fact, as can be seen in figure 4(*b*), the finite length of the wires underestimates the total turbulence kinetic energy. The long wires from the 139-probe array resolve 60% of the total turbulence kinetic energy at 21 diameters, the missing portion having been removed by the spatial filtering of the long wires. Farther downstream, the resolution drops to 49% at 46 diameters away from the jet exit, 37% at 54 diameters, and a low 22% at 69 diameters. Despite this, the POD reconstructs the field properly (because it resolves the necessary modes), but a field that is truncated because of the experimental conditions. Simlarity considerations imply

$$E \equiv \sum_n \sum_m \int_f \lambda^{(n)}(m, f; x)\, \mathrm{d}f \propto U_c^2 \delta_{1/2}^2 \tag{6.2}$$

which, defining their ratio, implies

$$K \equiv \frac{\displaystyle\sum_n \sum_m \int_f \lambda^{(n)}(m, f; x)\, \mathrm{d}f}{U_c^2 \delta_{1/2}^2} = \text{constant}. \tag{6.3}$$

Tables 5 and 6 summarize the results for the different experimental configurations.

Since the variations of K are significant, $U_c^2\delta_{1/2}^2$ must be replaced by E in the non-dimensionalized plots to provide an appropriate comparison of the measured quantities. This can be easily seen in figure 7 where the azimuthal dependence of the first eigenspectrum is presented with the two different scalings: either with $U_c^2\delta_{1/2}^2$ (part *a*), or with the total energy seen by the array, $E \equiv \int_f \sum_n \sum_m \lambda^{(n)}(m, f; x)\, \mathrm{d}f$ (part *b*).

Figure 8 presents slices at constant azimuthal mode number for mode numbers 0, 1 and 2 which contain most of the energy. The collapse is excellent, proving not only that the POD is well resolved, but also that it agrees well with the equilibrium similarity theory. The influence of the difference in coverage of the array is seen to

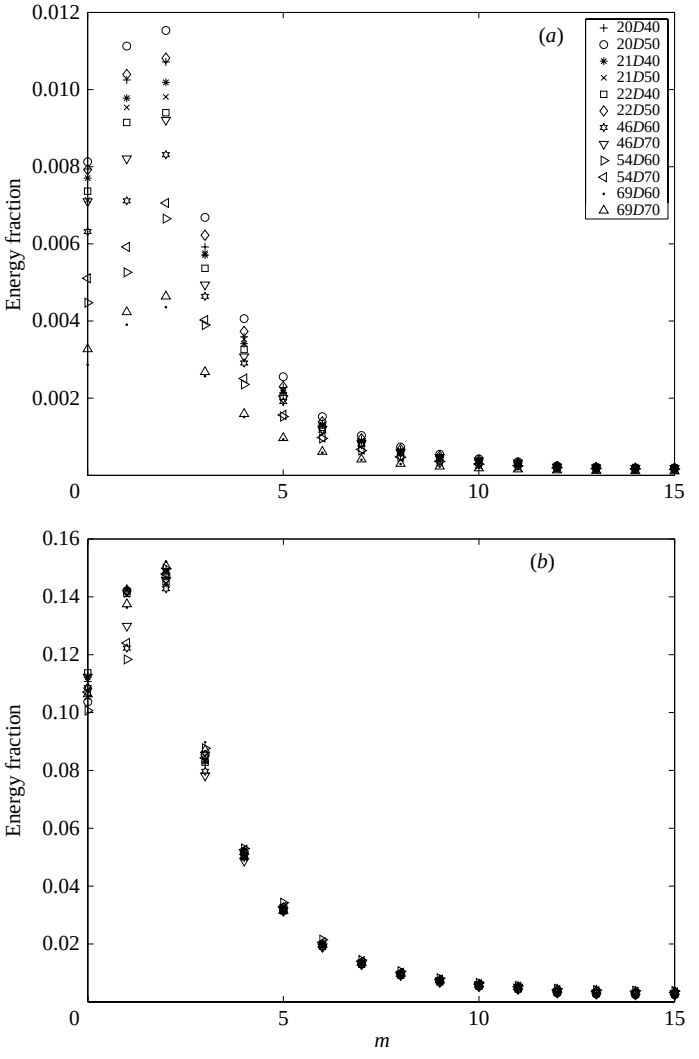

FIGURE 7. $\int \lambda^{(1)}(m, f; x)\,\mathrm{d}f$ non-dimensionalized for all the 139-hot-wire array configurations: (*a*) divided by $U_c^2\delta_{1/2}^2$, (*b*) divided by $E \equiv \int_f \sum_n \sum_m \lambda^{(n)}(m, f; x)\,\mathrm{d}f$.

affect mostly the amplitude of the peaks at azimuthal mode-0 and mode-1, as shown in Appendix B. As expected, the results farthest downstream are the most affected. The third peak at mode-0 for near-zero frequency disappears as the array moves downstream. Also, the secondary peak at mode-1 becomes more important as the coverage gets worse.

Equilibrium similarity thus provides a excellent tool to evaluate the effect of the different experimental conditions. Special care must be taken, however, when comparing the data from the two different hot-wire arrays with each other. Because of differences in array coverage and wire length, the arrays do not pick up the same amount of energy. This can be seen easily in the amount of energy recovered by the first POD mode: 63% for the long hot wires compared to 52% for the smaller ones. To compare the different sets, the CTH eigenspectra were multiplied by the average amount of energy picked up by the first eigenspectrum of the UB data, and then

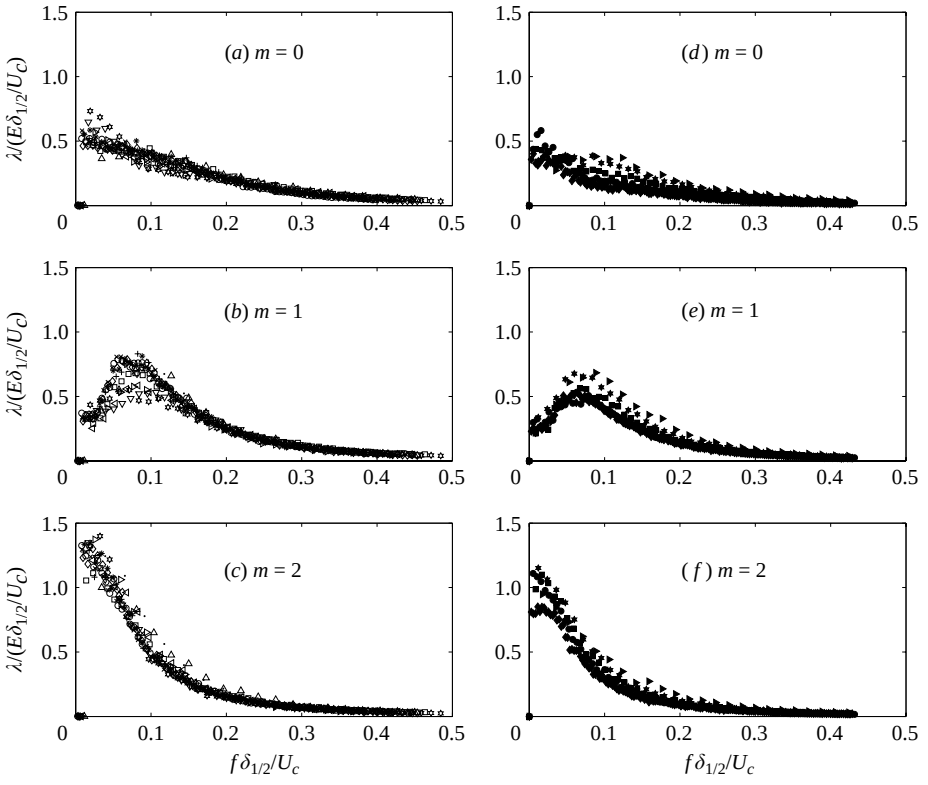

FIGURE 8. Slices at constant azimuthal mode numbers of the first eigenspectrum non-dimensionalized in similarity variables: (*a–c*) the 139-hot-wire array data (at $m = 0$, 1, and 2 respectively); (*d–f*) the 15-hot-wire array data (at $m = 0$, 1, and 2 respectively). For legend, see figure 4.

divided by the measured amount in the case of the CTH data shown in figure 9. The scatter is quite reasonable given the differences in experimental setups, as noted in § 5.1 above, and discussed in detail in Appendix B.

7. The eigenfunctions

The eigenfunctions are of considerable interest to theoreticians, so an effort to summarize their characteristics will be made here. Also, as noted in Part 1, these alone in the POD contain a dependence on the radial coordinate, r. In figures 10 and 11, the real and imaginary parts of the eigenfunctions of the first POD mode, $n = 1$, are plotted for two cases: 21 diameters at 50 m s^{-1}and 46 diameters at 70 m s^{-1}for the UB measurements. To facilitate the comparison, they were scaled using the similarity scaling described above. The first radius clearly dominates in most of the configurations, which certainly explains why the POD is so efficient despite the reduced outside coverage of the flow field at the extreme streamwise positions for each jet. The wavy behaviour of the eigenfunctions, especially with the relative importance of the first radius, is in qualitative agreement with that obtained by Michalke (1984) from linear stability theory.

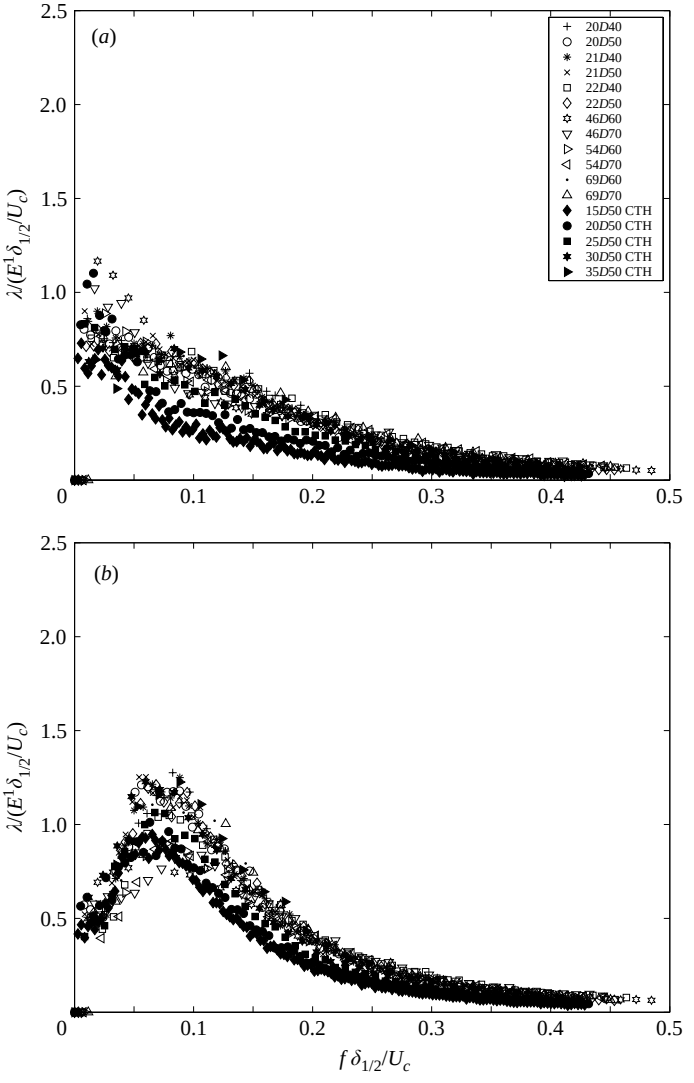

FIGURE 9(*a*, *b*). For caption see next page.

For the azimuthal mode-0 of the first POD mode (part (*a*) of figures 10 and 11), the real parts of the eigenfunctions exhibit quite a uniform behaviour over the frequency range, which is consistent with the fact that the corresponding eigenspectra have broad frequency characteristics. For near-zero frequency, however, the farthest position at 46 diameters has behaviour opposite to that at 21 diameters: mainly an increase in value as one moves farther from the centreline. This can be linked to the fact that the first eigenspectrum, $\lambda^{(1)}$, peaks at mode-0 and near-zero frequency at 46 diameters (figure 5 in § 5), while it does not at 21 diameters.

The same phenomenon also occurs for azimuthal mode-1. This seems to be a consequence of the change of scales seen by the array between the 2.54 cm and the 1 cm jet, as mentioned previously. The imaginary part of the eigenfunctions is almost zero, except for a narrow peak at the exact frequency peak of the eigenspectrum at azimuthal mode-1. This particular peak might be related to the Strouhal peak at

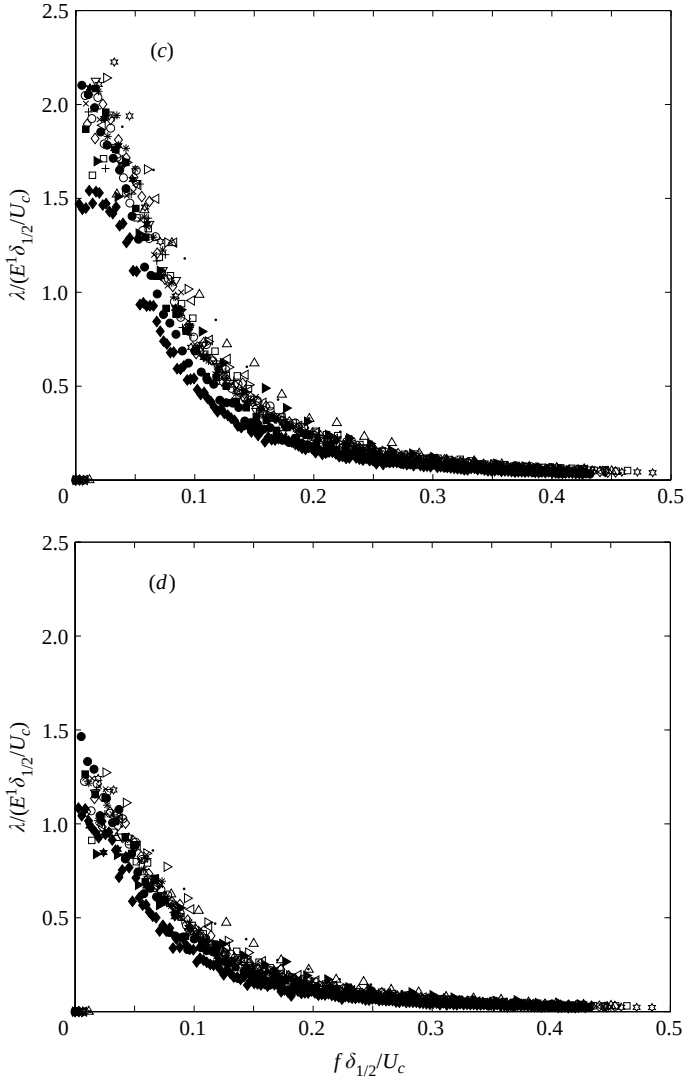

FIGURE 9. Eigenspectrum in non-dimensionalized variables as a function of non-dimensionalized frequency for different azimuthal mode numbers: (*a*) $m = 0$, (*b*) $m = 1$, (*c*) $m = 2$, and (*d*) $m = 3$. Amplitude of CTH data adjusted as mentioned in the text.

mode-1 in the eigenspectra. The real part of the eigenfunctions changes behaviour at the same frequency peak as the eigenspectra, but then it exhibits a second more extreme sharp evolution at a higher frequency, close to a harmonic of the peak for the eigenspectrum, $\lambda^{(1)}$, with a gain in importance of the inner radius. Afterwards they follow a rather smooth behaviour, similar to that for azimuthal mode-0.

The pattern for azimuthal mode-2 (part (*c*) figures 10 and 11) is more regular and shows that the eigenfunctions peak in the middle of the shear layer for low frequencies, then slowly evolve with frequency towards a dominance of the first radius as for the lower azimuthal mode numbers. The imaginary part has a rather smooth behaviour, similar to the real part at mode-0.

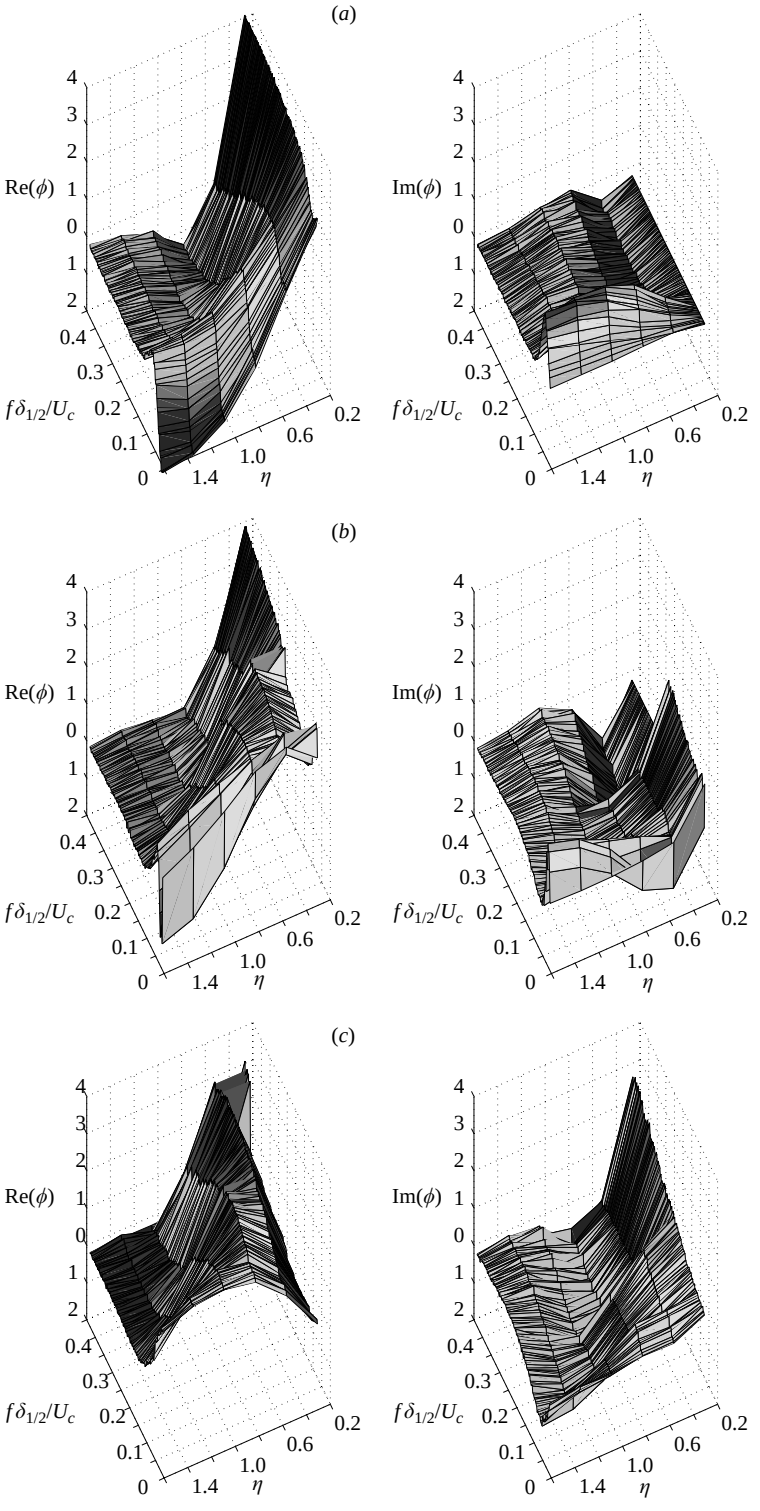

FIGURE 10. Non-dimensionalized eigenfunctions for the first POD mode at $21D$, 50 m s^{-1}. (*a*) Azimuthal mode-0, (*b*) mode-1, (*c*) mode-2.

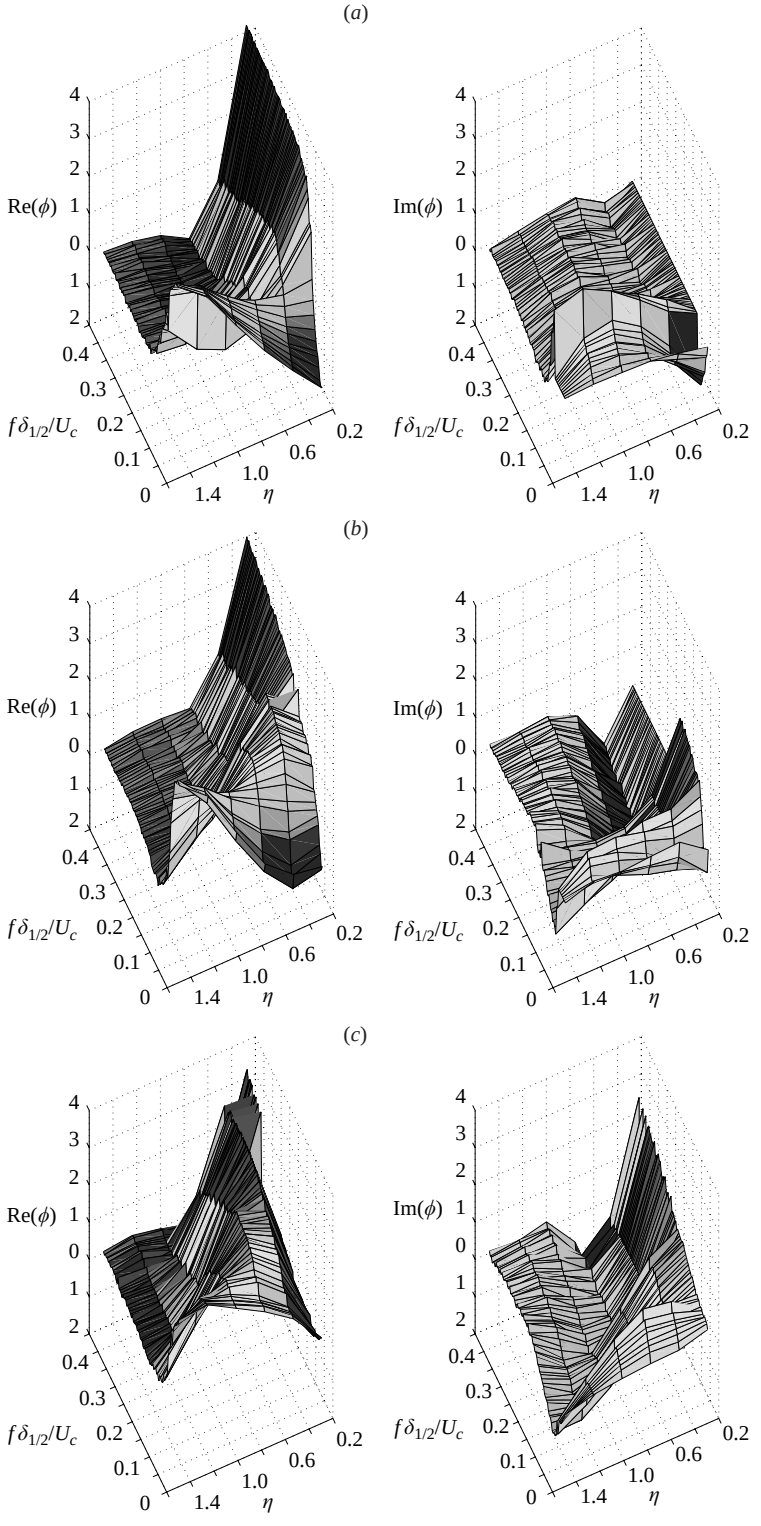

FIGURE 11. Non-dimensionalized eigenfunctions for the first POD mode at $46D$, 70 m s^{-1}. (*a*) Azimuthal mode-0, (*b*) mode-1, (*c*) mode-2.

8. Conclusion and discussion

Measurements in the far field of an axisymmetric turbulent jet were made with two different experimental techniques. The experiments covered a downstream distance from 15 to 69 diameters, and Reynolds numbers from 40 000 to 84 700. The POD was applied to 'slices' (or cross-sections) of the flow. The resulting eigenspectra show how the energy is partitioned in the flow. More than 50% of the resolved energy appeared in the first POD mode. The eigenspectrum for this first POD mode has three distinct peaks: a dominant one at azimuthal mode-2 for near zero frequency, another at azimuthal mode-1 for a constant local Strouhal number (fx/U_c) of approximately 1, and a third smaller peak at azimuthal mode-0 at near-zero frequency. Unlike the other two peaks, that at mode-1 seems to be a convected instability. The normalized eigenspectra did not depend on downstream distance in the equilibrium similarity region. They were also shown to collapse when scaled in the jet similarity variables, consistent with an equilibrium similarity analysis of the two-point equations. When integrated to remove the frequency dependence, and normalized by the streamwise component of the turbulence kinetic energy, the first eigenspectrum showed a clear dominance of azimuthal mode-2.

Surprisingly, the results were similar to experimental results taken at the end of the potential core by Jung *et al.* (2002) (see Part 1), well before the region of equilibrium similarity is supposed to apply. This predominance of azimuthal mode-2 in the far jet was first reported by Jung *et al.* (2002) and Gamard *et al.* (2002), and has since been confirmed independently by DNS computations, as reported by Freund & Colonius (2002). The evolution of the eigenspectra towards a dominance of azimuthal mode-2 seems also to be linked to the creation of acoustic noise in this flow, since V. F. Kopiev (2001, personal communication) discovered unexpected noise sources beyond $x/D = 5$ for mode-2.

Even more intriguing is that our results are very similar in behaviour to results obtained in the wake of an axisymmetric disk by Johansson, George & Woodward (2002). Although the wake is also a flow which admits equilibrium similarity solutions, the local Reynolds number decreases downstream, unlike the jet where it is constant. Thus the statistical axisymmetry of the flow appears to dominate all other considerations. Clearly a substantial advance in our theoretical understanding of circular, non-parallel and/or nonlinear flows, perhaps with a combination of spatially and temporal evolving theories, is required to understand these results, and understand the role and origin of the different frequency and azimuthal mode number peaks.

This work was initiated at the Turbulence Research Laboratory of the State University of New York at Buffalo (UB), and continued with the move of TRL to Chalmers University of Technology (CTH) in Gothenburg, Sweden. The bulk of the work in this paper is taken from the PhD dissertations of S. G. (Gamard 2002*a*, *b*). The support of the US Air Force Office of Scientific Research under grant number F49620-98-1-0143 and the US National Science Foundation under grant CTS-9102863 is gratefully acknowledged. The work was completed with the support of the Swedish Research Council under grant 2001-2641. The authors are very grateful to S. Woodward and L. Jernqvist for lending their technical expertise, and to Elteyeb Eljack, Peter B. V. Johansson and Professor Joran Bergh of Chalmers for their help and enlightening discussions regarding the many aspects of this work.

Appendix A. A brief history of mode-1

It is interesting to trace the history of how the experimental community came to believe that azimuthal mode-1 should dominate the far jet. Experimentalists appear to have limited their search for alternatives, citing the agreement with theory. Similarly, theoreticians limited the scope of their inquiries because of the apparent agreement with experiment. The idea appears to have originated with Batchelor & Gill (1962) who developed a stability analysis for temporal disturbances in a parallel axisymmetric jet. They showed that, in the potential core region of the jet where the mean profile has a flat region, the necessary condition for existence of an unstable disturbance is satisfied by all azimuthal mode numbers. In the far region, however, they used a velocity profile based on an eddy viscosity approximation, and concluded that only azimuthal mode-1 is unstable. No other mean velocity profiles were considered.

Others since have contributed, some agreeing, some not. Arguing that a spatially evolving disturbance is more appropriate, Michalke (1964) derived equations for an axisymmetric perturbation using an hyperbolic tangent profile. Michalke (1965) refined this analysis and compared it with measurements from a forcing experiment. Non-axisymmetric modes were added in Michalke (1984), and azimuthal mode-1 was also seen to dominate. Michalke remarked, however, without investigating much further that higher modes had an 'irregular' behaviour in some frequency ranges. Allowing for different widths of the shear layer at his computed downstream positions, Chan (1974) refined the spatially evolving problem. Chan (1977) used the energy equation and an eddy viscosity model, and found improvements to a diverging linear problem that compared favourably with pressure measurements of an acoustically forced jet. At his Strouhal forcing, azimuthal mode-0 was seen to dominate. Plascko (1979), however, using a multiple-scale expansion, concluded that the results were very much dependent on the value of the forcing frequency. Indeed, he showed that at a lower Strouhal number, azimuthal mode-1 overtook mode-0, proving that whichever mode dominated the flow really depended on the frequency.

Recently George, Johansson & Gamard (2002) re-considered the criteria of Batchelor & Gill (1962) for the propagation of the most unstable modes using different velocity profiles. They discovered, contrary to the earlier claims of these authors, that most velocity profiles used for the mean flow (and especially the ones best describing the behaviour of the axisymmetric jet), can allow neutral disturbances for any mode up to azimuthal mode-2 to dominate the flow field, in agreement with the POD experiments. Neutral disturbances for much higher modes are possible for the near jet. Even more recently, J.-M. Chomaz (2002, personal communication) has subjected these neutral disturbances to numerical analysis, and has concluded they do not grow. If this conclusion is substantiated, then the role and applicability of linear theory to the turbulent far jet is at best seriously in doubt. Regardless, this subject might evolve rapidly in the light of the experiments reported in this paper.

Appendix B. Influence of the coverage of the array

Due to the unexpected dominance of azimuthal mode-2 in the initial experiments, a test case was created to study the effects of the change of coverage of the flow field by the array. The articulated 15-wire array was placed at 10 diameters downstream of the jet exit, and measured for two conditions with roughly the same Reynolds number:

Case 1: Good array coverage. Jet diameter of 2.54 cm, exit velocity of 50 $\mathrm{m\,s^{-1}}$ ($Re_D = 85\,000$).

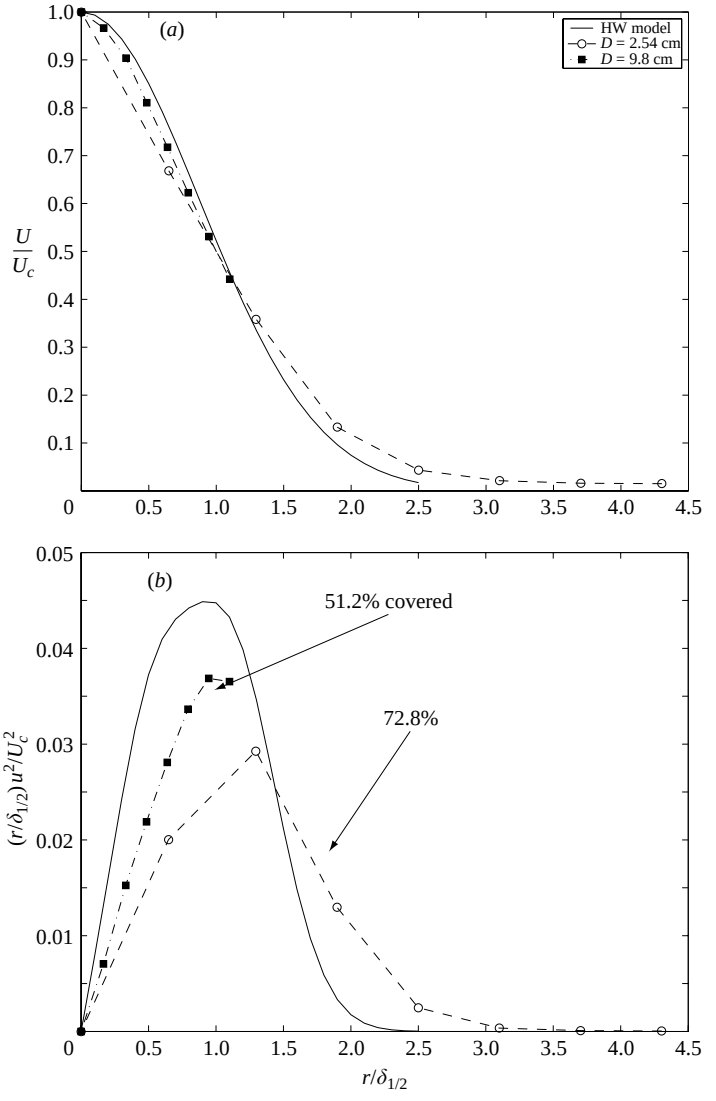

FIGURE 12. (*a*) Normalized mean velocity profiles at 10 diameters downstream with two different exit conditions compared with the analytical model taken from Hussein *et al.* (1994). (*b*) Integrands of the turbulence kinetic energy in similarity variables. Area under curve is the total streamwise turbulence kinetic energy in the flow. The ratios recovered by the wires, compared to the curve-fit of Hussein *et al.* (1994), are indicated.

Case 2: Bad array coverage. Jet diameter of 9.8 cm, exit velocity of 15 m s^{-1} ($Re_D = 98\,000$).

Figure 12 presents a summary of the single-point results. The probe positions relative to the mean velocity are clear from part (*a*): the first case spans only up to $\delta_{1/2}$, while the second case spans to $4.3\delta_{1/2}$. The resolution of the cross-section energy is shown in part (*b*) using the turbulence intensity profile of Hussein *et al.* (1994) for normalization. The modelled curve provides a reference to emphasize the different resolutions of the two test cases studied. Clearly a great deal of the energy is missing

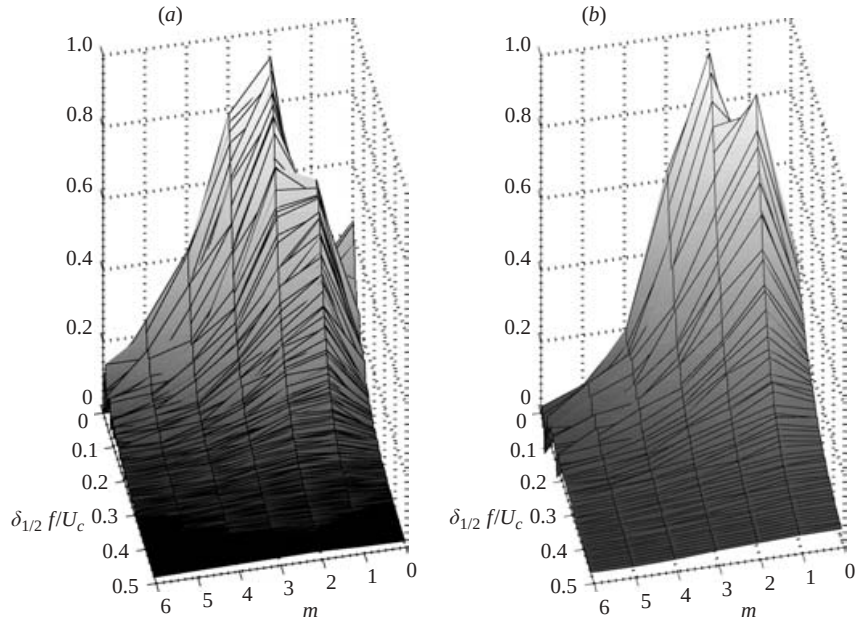

FIGURE 13. Normalized eigenspectra (for POD mode 1) in similarity variables at 10 diameters downstream. (*a*) Case 1: exit velocity of 50 m s^{-1}and diameter of 2.54 cm. (*b*) Case 2: exit velocity of 15 m s^{-1}, diameter of 9.8 cm.

for the bad coverage case due the absence of probes outside $r/\delta_{1/2} = 1$. By contrast, the good coverage case is missing a significant fraction of the energy near the core, due to the sparseness of probes in this region.

As in the main body of the paper, the POD was applied to the doubly Fourier transformed streamwise velocity cross-spectrum. Figure 13 presents the normalized eigenspectra for the first POD mode for the two test cases. There are significant differences in the two eigenspectra. The reduced total area coverage from the hot-wire array has the following consequences:

(i) The secondary peak at azimuthal mode-1 has increased in importance.
(ii) The tertiary peak at azimuthal mode-0 at near zero frequency has disappeared.
(iii) Azimuthal mode-3 has reduced amplitude at near-zero frequency.

The effect of such a difference in array coverage might seem quite benign, since the dominant peak for the eigenspectra has not changed, and is still at azimuthal mode-2 for near-zero frequency. The consequences are better seen, however, by focusing on only the azimuthal dependence of the eigenspectra (i.e. by integrating over frequency and normalizing by the total streamwise energy seen by the wires). Instead of having a preponderance of azimuthal mode-2 as before, figure 14 shows azimuthal mode-1 to be dominant.

Clearly extreme care must be taken in considering any data. The resolution (or lack of it) of the experimental technique plays a crucial role in determining which mode is actually dominating the energetics of the jet. It appears, in this case at least, that less than adequate coverage increases the importance of azimuthal mode-1 relative to mode-2. Thus the predominance of mode-2 in our experiments appears not to be an artifact of the experimental technique.

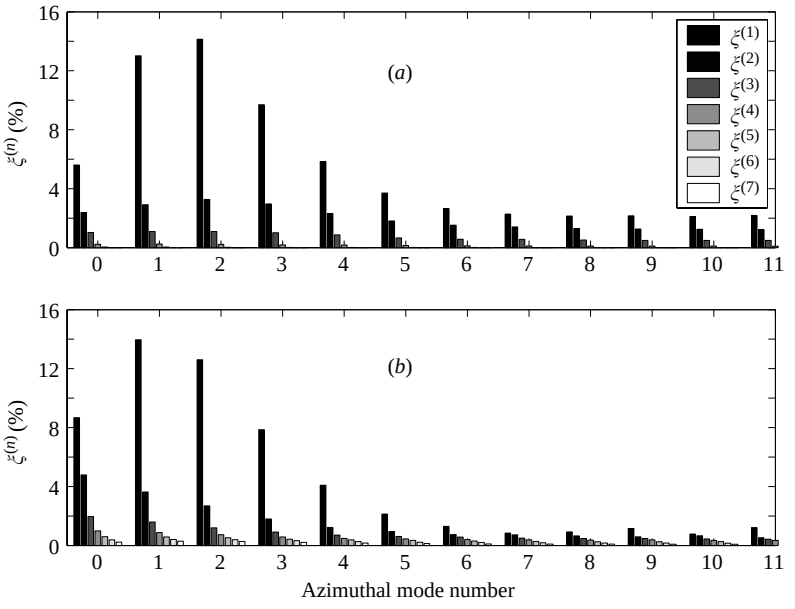

FIGURE 14. Normalized eigenspectra (for POD mode 1) in similarity variables at 10 diameters downstream. (*a*) Case 1: good array coverage. (*b*) Case 2: bad array coverage.

REFERENCES

BATCHELOR, G. K. & GILL, E. A. 1962 Analysis of the instability of axisymmetic jets. *J. Fluid Mech.* **14**, 529–551.

BOERSMA, G., BRETHOUWER, G. & NIEUWSTADT, F. 1998 A numerical investigation of the effect of inlet conditions on the self-similar region of a round jet. *Phys. Fluids* **10**, 899–909.

CHAN, Y. 1974 Spatial waves in turbulent jets. *Phys. Fluids* **17**, 46–53.

CHAN, Y. 1977 Wavelike eddies in a turbulent jet. *AIAA J.* **15**, 992–1001.

CITRINITI, J. H. & GEORGE, W. K. 1997 The reduction of spatial aliasing by long hot-wire anemometer probes. *Exps. Fluids* **23**, 217–224.

CITRINITI, J. H. & GEORGE, W. K. 2000 Reconstruction of the global velocity field in the axisymmetric mixing layer utilizing the proper orthogonal decomposition. *J. Fluid Mech.* **418**, 137–166.

DIMOTAKIS, P. E., MIAKE-LYE, R. C. & PAPANTONIOU, D. A. 1983 Structure and dynamics of round turbulent jets. *Phys. Fluids* **26**, 3185–3192.

EWING, D. 1995 On multi-point similarity solutions in turbulent free shear flows. PhD thesis, State University of New York at Buffalo.

EWING, D. & GEORGE, W. K. 1995 Similarity analysis of the two-point velocity correlation tensor in a turbulent axisymmetric jet. In *Turbulence, Heat, and Mass Transfer I* (ed. K. Hanjalic & J. C. F. Pereira), pp. 49–56. Begell House.

FREUND, J. B. & COLONIUS, T. 2002 POD analysis of sound generation by a turbulent jet. *AIAA Paper* 2002-0072.

GAMARD, S. 2002*a* Application of the POD to the far jet. PhD thesis, State University of New York at Buffalo.

GAMARD, S. 2002*b* The axisymmetric turbulent jet. PhD thesis, Chalmers University of Technology, Gothenburg, Sweden.

GAMARD, S., GEORGE, W. K., JUNG, D. & WOODWARD, S. 2002 Application of a 'slice' POD to the far field of an axisymmetric turbulent jet. *Phys. Fluids* **14**, 2515–2522.

GEORGE, W. K. 1988 Insight into the dynamics of coherent structures from a proper orthogonal decomposition. In *the Structure of Near Wall Turbulence, Proc. of Symp. on Near Wall Turbulence, Dubrovnik, Yugoslavia* (ed. S. Kline), pp. 168–180. Hemisphere.

George, W. K. 1989 The self-preservation of turbulent flows and its relation to initial conditions and coherent structures. In *Advances in Turbulence* (ed. W. K. George & R. E. A. Arndt), pp. 39–73. Hemisphere.

George, W. K. 1999 Some thoughts on similarity, the POD, and finite boundaries. In *Fundamental Problematic Issues in Turbulence* (ed. A. Gyr, W. Kinzelbach & A. Tsinober), pp. 117–128. Birkhauser.

George, W. K., Hussein, H. J. & Woodward, S. H. 1989 An evaluation of the effect of fluctuating convection velocity on the validity of Taylor's hypothesis. In *Proc. 10th Australasian Fluid Mechanics Conference V. II* (ed. A. Perry *et al.*), pp. 11.5–11.8. University of Melbourne.

George, W. K., Johansson, P. & Gamard, S. 2002 How has the study of coherent structures contributed to our understanding of turbulent free shear flows? In *Proc. FEDSM'02, Montreal*. ASME, Paper no. FEDSM2002-31408, pp. 1–10.

Glauser, M. N. 1987 Coherent structures in the axisymmetric turbulent jet mixing layer. PhD thesis, State University of New York at Buffalo.

Holmes, P., Lumley, J. L. & Berkooz, G. 1996 *Turbulence, Coherent Structures, Symmetry and Dynamical Systems*. Cambridge University.

Huerre, P. & Monkewitz, P. 1990 Local and global instabilities in spatially developing flows. *Annu. Rev. Fluid Mech.* **22**, 473–537.

Hussein, H. J., Capp, S. P. & George, W. K. 1994 Velocity measurements in a high-Reynolds-number, momentum-conserving, axisymmetric, turbulent jet. *J. Fluid Mech.* **258**, 31–75.

Johansson, P. B. V., George, W. K. & Woodward, S. H. 2002 Proper orthogonal decomposition of an axisymmetric turbulent wake behind a disk. *Phys. Fluids* **14**, 2508–2514.

Jung, D. 2001 An investigation of the Reynolds-number dependence of the axisymmetric jet mixing layer using a 138 hot-wire probe and the POD. PhD thesis, State University of New York at Buffalo.

Jung, D., Gamard, S. & George, W. 2004 Downstream evolution of the most energetic modes in a turbulent axisymmetric jet at high Reynolds number. Part 1. The near-field region. *J. Fluid Mech.* **514**, 173–204.

Jung, D., Gamard, S., Woodward, S. H. & George, W. K. 2002 Downstream evolution of the most energetic pod modes in the mixing layer of a high reynolds number axisymmetric jet. In *Turbulent Mixing and Combustion. Proc. IUTAM Symp. Queen's University, Kingston, ON, CA*. (ed. A. Pollard & S. Candel), pp. 23–32. Kluwer.

Kopiev, V. F., Zaitsev, M. Y., Chernyshev, S. A. & Kotova, A. N. 1999 The role of large-scale vortex in a turbulent jet noise. *AIAA Paper* 99-1839.

Lumley, J. L. 1965 On the interpretation of time spectra in high intensity shear flows. *Phys. Fluids* **8**, 1056–1062.

Mi, J., Nobes, D. & Nathan, G. 2001 Influence of jet exit conditions on the passive scalar field of an axisymmetric free jet. *J. Fluid Mech.* **432**, 91–125.

Michalke, A. 1964 On the inviscid instability of the hyperbolic-tangent velocity profile. *J. Fluid Mech.* **19**, 543–556.

Michalke, A. 1965 On spatially growing disturbances in an inviscid shear layer. *J. Fluid Mech.* **23**, 521–544.

Michalke, A. 1984 Survey on jet instability theory. *Prog. Aerospace Sci.* **21**, 159–199.

Mungal, M. G. & Hollingsworth, D. K. 1989 Organized motion in a very high Reynolds number jet. *Phys. Fluids* A **1**, 1615–1623.

Panchapakesan, N. R. & Lumley, J. L. 1993 Turbulence measurements in axisymetric jets of air and helium. Part 2. Helium jets. *J. Fluid Mech.* **246**, 225–247.

Plascko, P. 1979 Helical instabilities of slowly diverging jets. *J. Fluid Mech.* **92**, 209–216.

Tso, J. & Hussain, F. 1989 Organized motions in a fully developed turbulent axisymmetric jet. *J. Fluid Mech.* **203**, 425–448.

Wills, J. A. B. 1964 On convection velocities in turbulent shear flows. *J. Fluid Mech.* **20**, 417–432.

Yoda, M., Hesselink, L. & Mungal, M. G. 1992 The evolution and nature of large-scale structures in the turbulent jet. *Phys. Fluids* A **4**, 803–811.

Yoda, M., Hesselink, L. & Mungal, M. G. 1994 Instantaneous three-dimensional concentration measurements in the self-similar region of a round high-Schmidt-number jet. *J. Fluid Mech.* **279**, 313–350.

Zaman, K. B. M. Q. & Hussain, A. K. M. F. 1981 Taylor hypothesis and large-scale coherent structures. *J. Fluid Mech.* **112**, 379–396.